LETTER

doi:10.1038/nature12827

Increased insolation threshold for runaway greenhouse processes on Earth-like planets

Jérémy Leconte[1], Francois Forget[1], Benjamin Charnay[1], Robin Wordsworth[2] & Alizée Pottier[1]

The increase in solar luminosity over geological timescales should warm the Earth's climate, increasing water evaporation, which will in turn enhance the atmospheric greenhouse effect. Above a certain critical insolation, this destabilizing greenhouse feedback can 'run away' until the oceans have completely evaporated[1–4]. Through increases in stratospheric humidity, warming may also cause evaporative loss of the oceans to space before the runaway greenhouse state occurs[5,6]. The critical insolation thresholds for these processes, however, remain uncertain because they have so far been evaluated using one-dimensional models that cannot account for the dynamical and cloud feedback effects that are key stabilizing features of the Earth's climate. Here we use a three-dimensional global climate model to show that the insolation threshold for the runaway greenhouse state to occur is about 375 W m^{-2}, which is significantly higher than previously thought[6,7]. Our model is specifically developed to quantify the climate response of Earth-like planets to increased insolation in hot and extremely moist atmospheres. In contrast with previous studies, we find that clouds have a destabilizing feedback effect on the long-term warming. However, subsident, unsaturated regions created by the Hadley circulation have a stabilizing effect that is strong enough to shift the runaway greenhouse limit to higher values of insolation than are inferred from one-dimensional models. Furthermore, because of wavelength-dependent radiative effects, the stratosphere remains sufficiently cold and dry to hamper the escape of atmospheric water, even at large fluxes. This has strong implications for the possibility of liquid water existing on Venus early in its history, and extends the size of the habitable zone around other stars.

Planetary atmospheres naturally settle into a thermal equilibrium state where their outgoing thermal emission balances the absorbed part of the incoming sunlight. The resulting climate is stabilized by the fact that a temperature increase results in enhanced cooling by means of thermal emission. When a condensable greenhouse gas is present at the planet's surface, as is the case for water on the Earth, this stabilizing feedback is hampered by the destabilizing greenhouse feedback: evaporation and, thus, the water-vapour greenhouse effect increase with temperature, reducing the cooling. Under present Earth conditions, this greenhouse feedback is both strong enough to maintain clement surface temperatures and weak enough for the climate to remain stable.

When solar heating becomes stronger, however, water vapour can become abundant enough to make the atmosphere optically thick at all thermal wavelengths[7,8]. Thermal flux then originates in the upper troposphere only and reaches a maximum, ~282 W m^{-2}, that is independent of the surface temperature[9]. If the planet absorbs more than this critical flux, thermal equilibrium can be restored only by vaporizing all the water available and reaching high surface temperatures at which the surface starts to radiate at visible wavelengths[4,7]. This is the runaway greenhouse state[1–4].

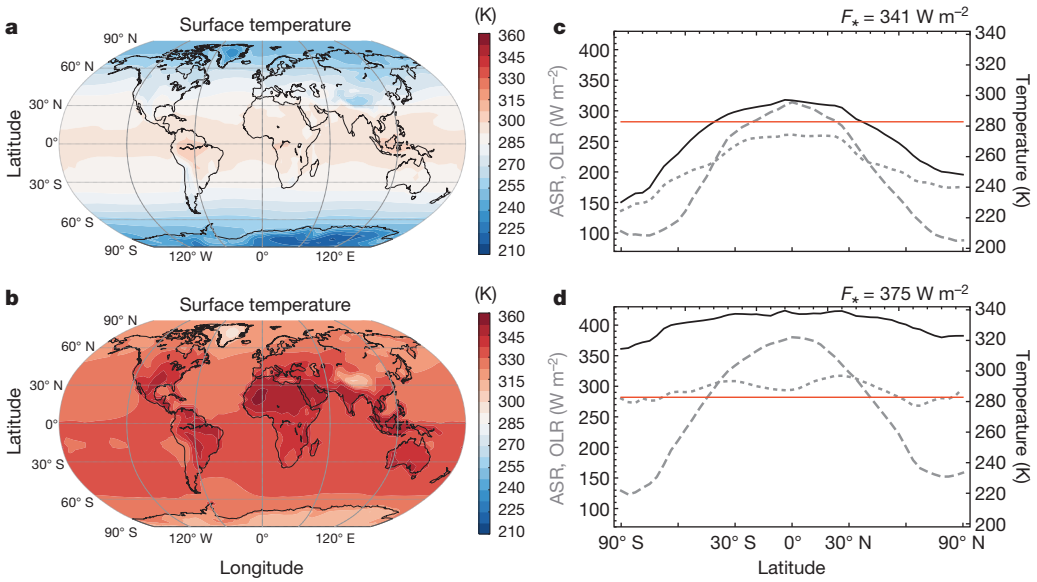

Figure 1 | Temperature and radiative budget for the Earth under two insolations. **a**, **b**, Maps of the annual mean surface temperature for the models corresponding to present Earth ($F_\star$ = 341 W m^{-2}; **a**) and to a mean solar flux of 375 W m^{-2} (**b**), just before the runaway greenhouse instability is triggered. **c**, **d**, Zonally and annually averaged surface temperature (solid black), absorbed stellar radiation (ASR; grey dashed) and outgoing long-wave radiation (OLR; grey dotted) for the insolations in **a** (**c**) and **b** (**d**). The red horizontal line shows the radiation limit on the emitted flux for a saturated water atmosphere (282 W m^{-2}). As visible in the hot case, unsaturated subtropical regions allow the atmosphere to emit more than this limit.

[1]Laboratoire de Météorologie Dynamique, Institut Pierre Simon Laplace, 4 Place Jussieu, BP 99, 75252 Paris, France. [2]Department of Geological Sciences, University of Chicago, Chicago, Illinois 60637, USA.

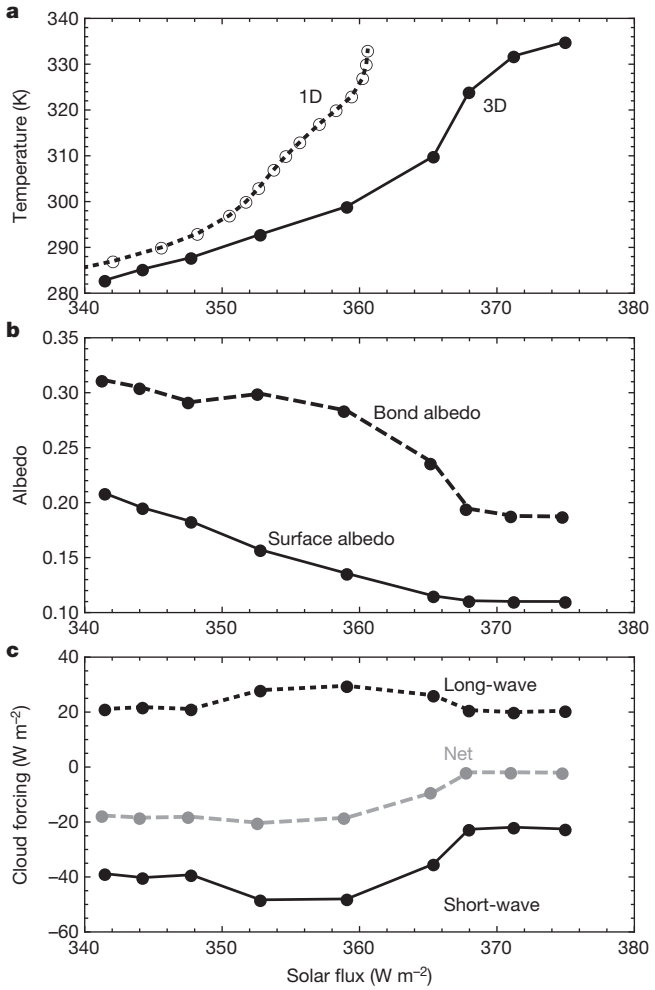

Figure 2 | Evolution of the mean surface temperature, planetary albedo and cloud radiative forcing with the mean solar incoming flux. Curves start from present Earth conditions (~341 W m^{-2}). **a**, Average surface temperature in our 3D baseline model (solid) and temperature in the 1D cloud-free model (dashed). **b**, Average surface albedo (solid) and effective planetary albedo (or Bond albedo; dashed). **c**, Short-wave (solid), long-wave (dotted) and net (grey dashed) cloud radiative forcing in the baseline model.

Because it has mostly been studied using one-dimensional (1D) atmosphere models, the aforementioned mechanism strongly relies on the assumption that the troposphere is saturated in water vapour. Furthermore, by construction, these studies could not account for spatial inhomogeneities in insolation and in the resulting water vapour and cloud distributions[4,6,7]. To overcome these limitations, we have developed a three-dimensional (3D) global climate model fit to describe hot atmospheres in which water vapour can become a dominant species[10–13] (Methods). The main challenges of such a model are threefold. First, the radiative transfer must be fast, yet able to describe accurately the spectroscopic properties of various gases in a wide temperature–pressure domain. Second, the modelling of the physical processes that are not specific to a given planet (convection, turbulence and so on) must rely on the fewest free parameters possible to ensure its validity under stringent conditions. Finally, for hot, moist atmospheres, the description of the water cycle (moist convection, cloud formation and so on) must take into account the fact that water can become a major constituent of the atmosphere. For these reasons, the global climate models usually used to predict Earth climate are generally not suited for such studies.

Here we perform simulations of future Earth climate by running our baseline model for various (increasing) values of the solar constant until radiative balance is achieved. For the present solar flux ($F_\star \approx 341$ W m^{-2}), our generic model reproduces the energy budget and the characteristics of our climate[13] (Fig. 1). When the flux is increased, the planet undergoes a decrease in surface albedo that is due to the melting of the permanent polar ice caps and the reduced seasonal snow cover (Fig. 2). For fluxes greater than ~350 W m^{-2}, only seasonal ice caps appear during the polar night. The amount of water vapour also increases. This results in a more efficient absorption of the incoming stellar light, but also in an enhanced greenhouse effect, which tends to homogenize the surface temperatures. Although continental surfaces can reach temperatures of around 100 °C because of the intense solar and greenhouse heating, sea surface temperatures remain moderate with a small diurnal variation because they are thermodynamically controlled by latent heat cooling[14]. Finally, for fluxes greater than ~375 W m^{-2}, no thermal equilibrium exists. Although surface temperature increases with time, thermal emission reaches a limiting value. This is the onset of the runaway greenhouse instability.

This runaway greenhouse insolation threshold is greater than those recently found by previous 1D studies[6,7] and confirmed by our 1D model (Extended Data Fig. 1). To understand the mechanisms that increase this threshold in practice, we first analyse the radiative effect of clouds. Although 1D simulations cannot properly capture spatial variations in cloud distribution, it has been suggested that clouds should have a feedback effect that stabilizes the climate against the runaway greenhouse

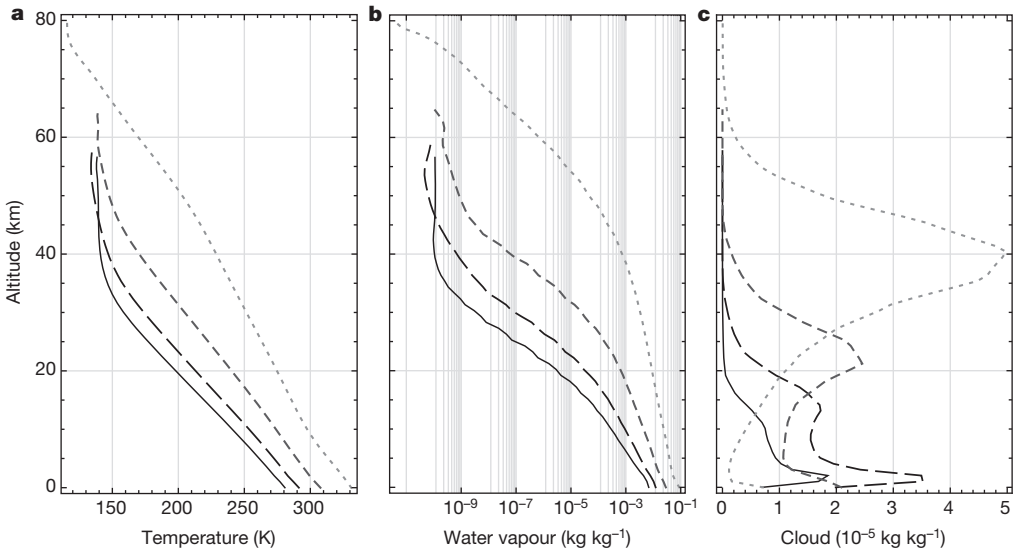

Figure 3 | Evolution of globally averaged vertical profiles. Mean vertical profiles of temperature (**a**) and water-vapour (**b**) and condensed-water (**c**) mixing ratios (in kilograms per kilogram of moist air in **b** and **c**) for four different insolations: 341 W m^{-2} (solid); 353 W m^{-2} (long dashed); 365 W m^{-2} (dashed); 375 W m^{-2} (dotted).

effect[4–6]. This tentative conclusion was based on the fact that the present net cloud radiative forcing on the Earth is negative, meaning that the albedo increase due to low-level clouds exceeds the greenhouse effect of high-level clouds[15]. Because of the increased evaporation resulting from the warming, cloud thickness might therefore increase and enhance the stabilizing effect of clouds[4–6].

Our simulations of the evolution of radiative cloud forcing with insolation suggest the opposite (Fig. 2c). This is due to a displacement of the cloud formation region towards higher altitudes (Fig. 3). As a result, the temperature at the mean cloud emission level increases much less with insolation than does the surface temperature. Even though the cloud optical depth increases, the greenhouse feedback of the clouds exceeds their albedo effect. At higher fluxes, clouds become thinner, which reduces both long-wave and short-wave radiative cloud forcing. For the reason described above, however, the greenhouse effect of clouds prevails and the net radiative forcing tends to vanish.

There are several reasons for the vertical displacement of clouds. First, moist convection and Hadley circulation become more intense as the insolation increases, extending the troposphere. Second, to form and persist, clouds need to be able to lose the latent heat released during condensation. Because of the infrared opacity increase of the atmosphere, the altitude at which clouds can efficiently cool radiatively rises. This may explain both the progressive disappearance of low-level clouds and the small change in cloud-deck temperature seen in Fig. 3.

Although the tendencies described above should be robust, the precise value of the cloud radiative forcing does depend on the assumptions made about the cloud microphysics. In our baseline model, for instance, we assume that the number density of cloud condensation nuclei, that is, the number of cloud particles per unit mass of air, remains fixed at a value that is representative of the modern Earth. As is expected, a larger mass mixing ratio of condensed water thus entails bigger cloud particles, which precipitate more easily and have a smaller radiative effect. To explore, and put limits on, the possible behaviour of clouds, we conducted a set of simulations in which the radii of cloud particles were kept constant. This assumption results in smaller radii, and thus overestimates cloud optical depths and both short- and long-wave cloud forcing. As can be seen in Extended Data Fig. 2, long-wave and short-wave forcing indeed increase continuously with insolation. However, for the reasons mentioned above, the greenhouse effect of clouds eventually overcomes the albedo effect. Therefore, the fact that the cloud feedback has a destabilizing effect under extreme insolation seems a robust conclusion, and one that supports results obtained in the context of anthropogenic global warming[16].

Clouds might not help stabilize climate against solar flux increases, but atmospheric dynamics does. This is due to the fact that when a parcel of moist air is heated without any source of moisture, its water vapour pressure decreases relative to the saturation pressure. As a result, the Earth's troposphere itself is not saturated everywhere, unlike what is often assumed in 1D models. An example of this are sub-tropical regions receiving hot air that comes from the Hadley cell, which dries during its ascent in the tropics and is compressed adiabatically during its descent[17] (Fig. 4). Because they stabilize the Earth's tropics today, such dynamically unsaturated regions where the water-vapour greenhouse effect is reduced stabilize the climate against the runaway greenhouse effect by playing the role of 'radiative fins' where the emission can locally exceed the maximum emission for a saturated atmosphere[18,19] (Fig. 1).

Furthermore, these unsaturated regions have the interesting property of extending upwards and polewards with the Hadley cell (Fig. 4), and of getting dryer when the insolation increases[17] (Extended Data Figs 3 and 4). Such unsaturated regions, which cannot be predicted using a 1D model, ensure that the infrared photosphere is always at a lower altitude than in the saturated case, yielding a more efficient cooling to space. This stabilizing feedback is the main reason why the runaway greenhouse insolation threshold predicted by 3D simulations is greater than previously found. And it would be even greater if it were not for the positive cloud feedback (Methods).

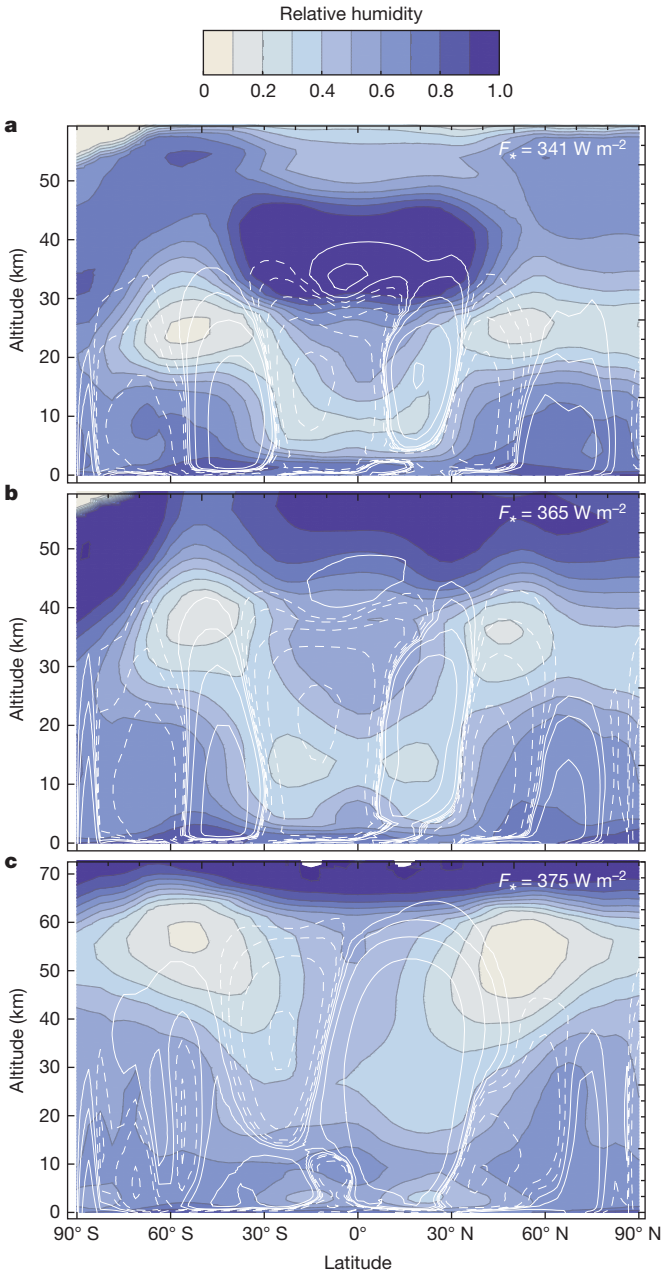

Figure 4 | Meridional distribution of relative humidity. Zonally and annually averaged relative humidity for models in which the respective stellar fluxes are 341 (**a**), 365 (**b**) and 375 (**c**) W m^{-2}. White contours are streamlines showing the Hadley circulation (solid and dashed curves depict clockwise and anticlockwise rotation, respectively).

With this new estimation, the inner edge of the habitable zone for Earth-like planets in the Solar System is pushed inwards to ~0.95 AU, which means that the Earth should not enter a runaway greenhouse state for at least another billion years[20]. However, the question of whether or not the warming-induced increase in the stratospheric temperature and humidity could cause the loss of the oceans to atmospheric escape before the runaway greenhouse instability is triggered, as suggested by some 1D studies[4,6], is still subject to debate. Our simulations tend to answer this question in the negative. This is due to both non-grey radiative effects[14,21,22] (Methods) and unsaturated regions that flatten the thermal profile in the troposphere. As a result, stratospheric temperatures are much lower than anticipated and stratospheric humidity cannot reach the threshold needed for efficient water photodissociation and escape of hydrogen to space (Fig. 3).

As well as extending the habitable zone[23] towards the Sun, our results, more notably, highlight the fact that global climate models are needed to understand subtle climate feedbacks resulting from the inhomogeneous insolation of planetary surfaces that are not amenable to 1D modelling. Although adding complexity and uncertainties, these subtle effects must be accounted for when modelling real planets, especially tidally synchronized exoplanets where they are even more pronounced[12,24,25]. In particular, although our simulation suggest that Venus, if it had the Earth's rotation rate, would have been in a runaway greenhouse state since its formation, its slow retrograde motion (because it results in a long Solar day) or a small water inventory[12,26] could completely change that view: both of these effects would tend to stabilize planetary climates against a runaway greenhouse state, respectively by increasing the albedo effect of clouds or by reducing the greenhouse effect of water vapour.

METHODS SUMMARY

Our simulations were performed with an upgraded version of the LMD generic global climate model specifically developed for the study of extrasolar planets[10,12,27] and palaeoclimates[11,28]. The model uses the 3D dynamical core of the LMDZ Earth global climate model used in studies by the Intergovernmental Panel on Climate Change studies[29], which is based on a finite-difference formulation of the primitive equations of geophysical fluid dynamics.

General physical processes relevant for present-day Earth—including ground thermal inertia and albedo (Extended Data Fig. 5), turbulent transport, dry convection, evaporation/condensation and precipitation—are parameterized in the most physically based way to ensure the robustness of the model under extreme conditions[13]. For the present study, special care has been taken to treat properly the situation in which water vapour can become a major constituent of the atmosphere. As detailed in Methods, the radiative transfer and moist convection scheme have been validated by recent 1D results for the hot, pure-water atmosphere regime (Extended Data Fig. 1). A numerical scheme accounting for change in atmospheric mass and surface pressure with water-vapour evaporation/condensation has also been implemented.

Online Content Any additional Methods, Extended Data display items and Source Data are available in the online version of the paper; references unique to these sections appear only in the online paper.

Received 13 August; accepted 4 November 2013.

1. Simpson, G. C. Some studies in terrestrial radiation. *Mem. R. Meteorol. Soc.* **11,** 69–95 (1927).
2. Komabayashi, M. Discrete equilibrium temperatures of a hypothetical planet with the atmosphere and the hydrosphere of one component-two phase system under constant solar radiation. *J. Meteorol. Soc. Jpn* **45,** 137–138 (1967).
3. Ingersoll, A. P. The runaway greenhouse: a history of water on Venus. *J. Atmos. Sci.* **26,** 1191–1198 (1969).
4. Kasting, J. F., Pollack, J. B. & Ackerman, T. P. Response of Earth's atmosphere to increases in solar flux and implications for loss of water from Venus. *Icarus* **57,** 335–355 (1984).
5. Kasting, J. F. Runaway and moist greenhouse atmospheres and the evolution of Earth and Venus. *Icarus* **74,** 472–494 (1988).
6. Kopparapu, R. K. *et al.* Habitable zones around main-sequence stars: new estimates. *Astrophys. J.* **765,** 131 (2013).
7. Goldblatt, C., Robinson, T. D., Zahnle, K. J. & Crisp, D. Low simulated radiation limit for runaway greenhouse climates. *Nature Geosci.* **6,** 661–667 (2013).
8. Goldblatt, C. & Watson, A. J. The runaway greenhouse: implications for future climate change, geoengineering and planetary atmospheres. *Phil. Trans. R. Soc. Lond. A* **370,** 4197–4216 (2012).
9. Nakajima, S., Hayashi, Y.-Y. & Abe, Y. A study on the 'runaway greenhouse effect' with a one-dimensional radiative-convective equilibrium model. *J. Atmos. Sci.* **49,** 2256–2266 (1992).
10. Wordsworth, R. D. *et al.* Gliese 581d is the first discovered terrestrial-mass exoplanet in the habitable zone. *Astrophys. J.* **733,** L48 (2011).
11. Forget, F. *et al.* 3D modelling of the early Martian climate under a denser CO_2 atmosphere: temperatures and CO_2 ice clouds. *Icarus* **222,** 81–99 (2013).
12. Leconte, J. *et al.* 3D climate modeling of close-in land planets: circulation patterns, climate moist bistability, and habitability. *Astron. Astrophys.* **554,** A69 (2013).
13. Charnay, B. *et al.* Exploring the faint young Sun problem and the possible climates of the Archean Earth with a 3D GCM. *J. Geophys. Res.* **118,** 414–431 (2013).
14. Pierrehumbert, R. T. *Principles of Planetary Climate* 289–299 (Cambridge Univ. Press, 2010).
15. Ramanathan, V. *et al.* Cloud-radiative forcing and climate: results from the Earth radiation budget experiment. *Science* **243,** 57–63 (1989).
16. Soden, B. J. & Held, I. M. An assessment of climate feedbacks in coupled ocean atmosphere models. *J. Clim.* **19,** 3354–3360 (2006).
17. Sherwood, S. C. *et al.* Relative humidity changes in a warmer climate. *J. Geophys. Res.* **115,** D09104 (2010).
18. Pierrehumbert, R. T. Thermostats, radiator fins, and the local runaway greenhouse. *J. Atmos. Sci.* **52,** 1784–1806 (1995).
19. Ishiwatari, M., Takehiro, S.-I., Nakajima, K. & Hayashi, Y.-Y. A numerical study on appearance of the runaway greenhouse state of a three-dimensional gray atmosphere. *J. Atmos. Sci.* **59,** 3223–3238 (2002).
20. Gough, D. O. Solar interior structure and luminosity variations. *Sol. Phys.* **74,** 21–34 (1981).
21. Arking, A. & Grossman, K. The influence of line shape and band structure on temperatures in planetary atmospheres. *J. Atmos. Sci.* **29,** 937–949 (1972).
22. Wordsworth, R. & Pierrehumbert, R. T. Water loss from terrestrial planets with CO_2-rich atmospheres. *Astrophys. J.* **778,** 154 (2013).
23. Kasting, J. F., Whitmire, D. P. & Reynolds, R. T. Habitable zones around main sequence stars. *Icarus* **101,** 108–128 (1993).
24. Pierrehumbert, R. T. A palette of climates for Gliese 581g. *Astrophys. J.* **726,** L8 (2011).
25. Yang, J., Cowan, N. B. & Abbot, D. S. Stabilizing cloud feedback dramatically expands the habitable zone of tidally locked planets. *Astrophys. J.* **771,** L45 (2013).
26. Abe, Y., Abe-Ouchi, A., Sleep, N. H. & Zahnle, K. J. Habitable zone limits for dry planets. *Astrobiology* **11,** 443–460 (2011).
27. Selsis, F., Wordsworth, R. D. & Forget, F. Thermal phase curves of nontransiting terrestrial exoplanets. I. Characterizing atmospheres. *Astron. Astrophys.* **532,** A1 (2011).
28. Wordsworth, R. *et al.* Global modelling of the early Martian climate under a denser CO_2 atmosphere: water cycle and ice evolution. *Icarus* **222,** 1–19 (2013).
29. Hourdin, F. *et al.* The LMDZ4 general circulation model: climate performance and sensitivity to parametrized physics with emphasis on tropical convection. *Clim. Dyn.* **27,** 787–813 (2006).

Acknowledgements We thank our referees, J. Kasting and Y. Abe, for their thorough review, and A. Spiga and F. Selsis for discussions. This work was supported by grants from Région Ile-de-France.

Author Contributions J.L. developed the 'high temperature/humidity' version of the generic global climate model, performed the calculations, and led the analysis and writing of the results. F.F. initiated the development of the generic global climate model and provided critical advice during analysis and writing. B.C. worked on the development of the model and helped perform the comparison with present Earth climatology. R.W. developed the original version of the generic model and implemented the radiative transfer scheme. A.P. performed comparison runs and sensitivity studies. All the authors commented on the manuscript.

Author Information Reprints and permissions information is available at www.nature.com/reprints. The authors declare no competing financial interests. Readers are welcome to comment on the online version of the paper. Correspondence and requests for materials should be addressed to J.L. (jeremy.leconte@lmd.jussieu.fr).

METHODS

Numerical climate model. Our simulations were performed with an upgraded version of the LMD generic global climate model (GCM) specifically developed for the study of extrasolar planets[10,12,27] and palaeoclimates[11,28]. The model uses the 3D dynamical core of the LMDZ Earth GCM used in IPCC studies[29], based on a finite-difference formulation of the primitive equations of geophysical fluid dynamics.

A horizontal resolution of 64×48, corresponding to resolutions of 3.75° latitude by 5.625° longitude, is used for the simulations. The vertical grid uses hybrid coordinates: a terrain-following σ coordinate system in the lower atmosphere (σ being equal to the pressure divided by the surface pressure), and pressure levels in the upper atmosphere. In this work, we used 30 layers, with the lowest mid-layer level at 4 m and the top mid-layer level at 1 mbar. The time step used in the dynamical core is 90 s, and the tendencies given by the physical parameterizations and the radiative transfer are updated every 15 and 90 min, respectively.

The boundary-layer dynamics is accounted for by the time-dependent 2.5-level closure scheme of ref. 30, plus a convective adjustment which rapidly mixes the atmosphere in the case of dry unstable temperature profiles. Turbulence and convection mix energy (potential temperature), momentum (wind) and water (condensed and gaseous). A standard roughness coefficient of $z_0 = 10^{-2}$ m is used for both rocky and ocean surfaces, for simplicity.

The evolution of surface temperature is governed by the balance between radiative, latent and sensible heat fluxes (direct solar insolation, thermal radiation from the atmosphere and the surface, and turbulent and latent heat fluxes; see the discussion of the water cycle below) and thermal conduction in the soil. The parameterization of this last process is based on a 13-layer soil model solving the heat diffusion equation using finite differences. The depths of the layers were chosen to capture diurnal thermal waves as well as the deeper annual thermal wave. A vertically homogeneous soil is assumed. The thermal inertia of the continental surface is set to 2,000 J s$^{-1/2}$ m^{-2} K^{-1}. To model the high thermal inertia due to mixing in the upper layers of the oceans, the thermal inertia of the oceans is set to 18,000 J s$^{-1/2}$ m^{-2} K^{-1}. The albedo surface map used in this work is shown in Extended Data Fig. 5

Radiative transfer. The method used to produce our radiative transfer model is similar to that described in refs 10, 12. For a gaseous composition similar to the Earth (1 bar of N_2 with 376 p.p.m.v. of CO_2 and a variable amount of water vapour; CH_4, O_2 and O_3 have been discarded for more generality), we computed high-resolution spectra over a range of temperatures and pressures using the HITRAN 2008 database[31]. For this study, we used temperature and pressure grids with values $T = \{110, 170, \ldots, 710\}$ K, $P = \{10^{-3}, 10^{-2}, \ldots, 10^{5}\}$ mbar. The H_2O volume mixing ratio could vary in the range $\{10^{-7}, 10^{-6}, \ldots, 1\}$. The H_2O lines were truncated at 25 cm^{-1}, and the water-vapour continuum was included using the CKD model[32]. We also account for opacity due to N_2–N_2 collision-induced absorption[33,34].

The 'correlated-k' method was then used to produce a smaller database of coefficients suitable for fast calculation in a GCM. Owing to the linearity of the Schwarzschild equation of radiative transfer, the respective contributions of the thermal emission and downwelling stellar radiation can be treated separately, even in the same spectral channel. We therefore do not assume any spectral separation between the stellar and planetary emission wavelengths. For thermal emission, the model uses 19 spectral bands, and the two-stream equations are solved using the hemispheric mean approximation[35]. Absorption and scattering of the downwelling stellar radiation is treated with the δ-Eddington approximation within 18 bands. Sixteen points are used for the $\bar{g}$-space integration, where $\bar{g}$ is the cumulated distribution function of the absorption data for each band. Rayleigh scattering by N_2 and H_2O molecules is included using the method described in ref. 36 with an updated cross-section for water[37].

Water cycle. In the atmosphere, we follow the evolution of water in its vapour and condensed phases. These tracers are advected by the dynamical core, mixed by turbulence and dry and moist convection. Much care has been devoted to developing a robust and numerically stable water-cycle scheme that is accurate both in the trace gas (water-vapour mass mixing ratio $q_v \ll 1$) limit and the dominant gas ($q_v \approx 1$) limit. In particular, the atmospheric mass and surface pressure variation (and the related vertical transport of tracers through pressure levels) due to any evaporation, sublimation or condensation of water vapour is taken into account, as we now explain.

Cloud formation is treated using the prognostic equations of ref. 38. For each column and level, this scheme provides the cloud fraction, f_c, and the mass mixing ratio of condensed water, q_c, which are both functions of q_v and the saturation vapour mass mixing ratio, q_s. In addition, when part of a column reaches both 100% saturation and a super-moist-adiabat lapse rate, moist convective adjustment is performed following ref. 39, and the cloud fraction is set to unity. This moist-convection scheme has been chosen instead of more refined ones because it is more robust for a wide range of temperatures, at the cost of giving enhanced precipitation at the equator[40]. Furthermore, the moist-adiabat lapse rate has been generalized to account for the fact that water can be a dominant species. This yields

$$\frac{\partial \ln T}{\partial \ln p}\Big|_{\mathrm{moist}} = \frac{p}{p-p_v}\left((1-q_v)R_a + \frac{q_v L_v}{T}\right) \times \left(q_v c_{p,v} + q_a c_{p,a} + q_c c_{p,c} + q_v \frac{L_v}{T}\frac{p}{p-p_v}\frac{\mathrm{d}\ln p_s}{\mathrm{d}\ln T}\right)^{-1} \quad (1)$$

where p_i, M_i, $c_{p,i}$ and $R_i \equiv R^\star/M_i$ are respectively the pressures, molar masses, specific heat capacities at constant pressure and specific gas constants of the various phases (non-condensable gas, or air, denoted with a subscript a; condensable gas, or vapour, denoted by v; condensed material, denoted by c); p and T are respectively the total pressure and temperature; $R^\star$ is the molar ideal gas constant; L_v is the specific latent heat of vaporization; and p_s is the water-vapour saturation pressure.

In our baseline model, the liquid or icy water (depending on the temperature) is assumed to condense on a number, N_c, of activated cloud condensation nuclei (CCNs) per unit mass of moist air. This number density of CCNs is assumed to be spatially uniform but to have different values for liquid and ice cloud particles (the condensed-water phase is determined by the local temperature). Indeed, on the Earth, nucleation is found to be much less efficient in cold, high-level clouds, resulting in larger particle radii in these ice clouds than in liquid-water clouds. This dichotomy is essential to recover the observed balance between long-wave and short-wave cloud radiative forcings. To recover present Earth climate, the values used are 4×10^6 kg^{-1} for liquid-water clouds and 2×10^4 kg^{-1} for ice clouds.

Then the effective radius of the cloud particles is given by $r_{\mathrm{eff}} = (3q_c/4\pi\rho_c N_c)^{1/3}$, where ρ_c is the density of condensed water (10^3 kg m^{-3} for liquid and 920 kg m^{-3} for ice). In the special case where radii have been kept fixed, the values used were 12 and 38 μm for water droplets and ice particles, respectively. Precipitations are computed with the scheme given in ref. 41. Because this scheme explicitly considers the dependence on gravity, cloud particle radii and background air density, it should remain valid for a wide range of situations (see ref. 13 for details). Finally, the total cloud fraction of the column is assumed to be the cloud fraction of the level with the thickest cloud, and radiative transfer is computed both in the cloudy and clear sky regions. Fluxes are then linearly weighted between the two regions.

The ground is modelled using a simple bucket model with a maximal water capacity of 150 kg m^{-2}. When the water amount exceeds this limit, the surplus is regarded as runoff and added to the oceans. The effect of latent heat release during solidification or melting of snow or ice at the surface is taken into account. On the surface, ice can also have a radiative effect by linearly increasing the albedo of the ground to $A_{\mathrm{ice}} = 0.5$ until the ice surface density exceeds a certain threshold (here 30 kg m^{-2}).

Evaporation, E (in kg m^{-2} s^{-1}), is computed within the boundary-layer scheme, using a bulk aerodynamic formula multiplied by a dryness coefficient, β (which is zero for a dry surface and linearly increases to 1 when the water amount reaches 75 kg m^{-2} at the surface; $\beta = 1$ over oceans). This yields

$$E = \rho C V \beta \left[q_s(T_{\mathrm{surf}}) - q_v^1\right]$$

where ρ is the mass density of air, V is the wind speed above the surface, $q_s(T_{\mathrm{surf}})$ is the water-vapour mass mixing ratio at saturation at the surface, and q_v^1 is the mixing ratio in the first layer. The aerodynamic coefficient is given by $C = \kappa/\ln(1 + z_1/z_0)$, where $\kappa = 0.4$ is the Von Karman constant, z_0 is the roughness and z_1 is the altitude of the first level.

A numerical scheme for atmospheric mass redistribution due to the condensation of a non-trace gas. In most GCMs, when a trace gas condenses in a grid box, the variation in the total gas mass is neglected and the variation in the mass mixing ratio is given by $\delta q_v = \delta m_v / m_g$. Because water vapour is not a trace gas in our simulations, we must take into account this effect as well as the change in surface pressure (total mass of the atmosphere) entailed by the massive evaporation or condensation that can take place both at the surface and aloft. To that end, we developed a numerical scheme similar to the one used for CO_2 clouds on Mars[42]. This scheme can be used for any kind of condensing species without any assumptions on the mixing ratio of the vapour phase. The scheme is thus valid both in the trace- and dominant-gas limits as well as in intermediate regimes.

We developed the scheme in two steps. First, the various routines describing the water cycle (evaporation at the surface, moist convection, cloud condensation, precipitation) compute the mass of vapour that has been added at a level k, δm_v^k (which is greater than zero when vapour is created; δm_v^0 is the mass of water vapour evaporated directly at the ground), assuming that the gas mass in the layer is constant (usual approximation). Second, the change in the total pressure and mass mixing ratios due to the change in the total mass of gas (δm_g^k) is computed as follows.

For an atmospheric column of N layers and area A, the change in the surface pressure is given by

$$\delta p_s = \frac{g}{A}\sum_{k=0}^{N}\delta m_v^k \quad (2)$$

where g is the acceleration due to gravity. For the computation in each cell, the difficulty comes from the fact that we do not use Lagrangian coordinates. As a result, evaporation and condensation occurring both at the surface and aloft induce artificial mass fluxes through horizontal levels that must be accounted for.

For hybrid coordinates, as used in many GCMs, layer k encompasses the matter between $p^{k-1/2}$ and $p^{k+1/2}$, where $p^k \equiv \sigma^k p_s + \gamma^k$. The '$\sigma$ coordinates' are obtained by setting $\sigma^k \equiv p^k/p_s$ and $\gamma^k = 0$. Because both σ^k and γ^k are time independent, the variation in the gas mass in the layer during one time step is given by

$$\begin{aligned}\delta m_g^k &= \frac{A}{g}\left(\delta p^{k-1/2} - \delta p^{k+1/2}\right)\\ &= \frac{A}{g}\left(\sigma^{k-1/2} - \sigma^{k+1/2}\right)\delta p_s\end{aligned} \quad (3)$$

The variation in the gas mass in layer k is also linked to the mass flux through its interfaces ($W^{k-1/2}$ being the mass flux in kilograms between levels $k-1$ and k, which is taken to be positive when the flux is upward) by

$$\delta m_g^k = \delta m_v^k + W^{k-1/2} - W^{k+1/2} \quad (4)$$

Using equations (2)–(4), we can get a recursive formula for the fluxes

$$W^{k+1/2} = W^{k-1/2} + \delta m_v^k - \left(\sigma^{k-1/2} - \sigma^{k+1/2}\right)\sum_{k=0}^{N}\delta m_v^k$$

Because $W^{N+1/2} \equiv 0$, we can compute the other fluxes, and especially $W^{1/2} = \delta m_v^0$, since $\sigma^{1/2} \equiv 1$. Once the total mass fluxes are known, we can get the variation of the mixing ratios of the various tracers (generically called q here) by considering the tracer mass budget

$$\delta\left(m_g^k q^k\right) = q^{k-1/2}W^{k-1/2} - q^{k+1/2}W^{k+1/2} + \varepsilon\delta m_v^k \quad (5)$$

where $\varepsilon = 1$ if the tracer considered is the vapour phase of the condensing gas, $\varepsilon = -1$ if we consider the condensed phase and $\varepsilon = 0$ for every other tracer. The $q^{k-1/2}$ are the tracer mixing ratios transported through the interface $\sigma^{k-1/2}$. They are calculated using a 'Van-Leer I' finite volume transport scheme[43].

Alternatively, the tracer mass conservation can be written exactly, as

$$\delta\left(m_g^k q^k\right) = \left(m_g^k + \delta m_g^k\right)\delta q^k + q^k\delta m_g^k \quad (6)$$

where δq^k is the correction to be applied to the tracer mixing ratios. By combining equations (4)–(6), we can show that

$$\begin{aligned}\delta q^k = \frac{1}{m_g^k + \delta m_g^k}[&\left(q^{k-1/2} - q^k\right)W^{k-1/2}\\ &- \left(q^{k+1/2} - q^k\right)W^{k+1/2} + \left(\varepsilon - q^k\right)\delta m_v^k]\end{aligned}$$

where the first and second terms represent transport through σ levels and the third term corresponds to enrichment or depletion due to the variation of the gas mass.

Finally, apart from tracers, the mass of gas that is advected through levels also transports some energy and momentum. Once the mass fluxes have been computed, these exchanges are easily computed using

$$\begin{aligned}\delta u^k = \frac{1}{m_g^k\delta m_g^k}[&\left(u^{k-1/2} - u^k\right)W^{k-1/2}\\ &- \left(u^{k+1/2} - u^k\right)W^{k+1/2}]\end{aligned}$$

where we have shown an example for the zonal speed u, but equations are the same for other quantities.

Model validation at high temperatures. To validate both the radiative transfer and the implementation of the moist adiabat in very hot atmospheres, we have developed a 1D 'inverse climate modelling' version of our code, which has already been used in ref. 22. In its spirit, this model is very similar to the codes developed in refs 4, 6.

For a given surface temperature and background gas surface pressure, the vertical thermal and water-vapour profiles are integrated upwards following a moist-adiabat lapse rate (equation (1)) until a fixed stratospheric temperature is reached (here 200 K). Once the profile is built, the two-stream radiative transfer routine used in our full 3D GCM is used to compute the outgoing thermal radiation and the Bond albedo of the planet. In these calculations, the most important assumptions are that the planet is spherically symmetric with a fixed surface albedo, that the atmosphere is always saturated in water vapour and that the atmosphere is cloud free.

The results of this model are shown in Extended Data Fig. 1 for a surface albedo of 0.25 to be comparable with the recent results of ref. 7. We can see that the asymptotic behaviour of the thermal flux as well as its quantitative asymptotic value (282 W m^{-2}) are in good agreement with recently published similar models with up-to-date spectroscopic data[6,7,14]. Our albedo calculations show a discrepancy of less than 0.02 with respect to the relevant cases of ref. 7 (that is, the pure-water case and the transitional-atmosphere case with 1 bar N_2 and preindustrial CO_2). These small differences are of little importance given the uncertainties in the primary mechanism controlling the albedo, that is, the clouds.

Intrinsic 3D effects: the role of unsaturated regions. To gain more insight into the intrinsic differences between 1D and 3D simulations, we performed a set of idealized simulations. In this numerical experiment, we run our 3D model in a configuration without topography and with a uniform surface albedo. (The effect of ice albedo is not taken into account.) Furthermore, we do not take into account the radiative effect of clouds. Because we want to understand the role of the dynamically driven distribution of humidity, we treat the whole surface as an infinite reservoir of water. In these simulations, we are left with only one major free parameter (the background atmosphere being kept similar to the Earth's present atmosphere; see above): the surface albedo is fixed to 0.22 to recover a mean surface temperature similar to the Earth's under the present insolation.

The value of the mean surface temperature as a function of insolation is presented in Extended Data Fig. 3a. For comparison, we have computed the surface temperature given by our 1D model for the same surface albedo. Because we do not take into account both cloud forcing and ice albedo in this set of 3D simulations, the only differences between the two models are due to dynamical effects and horizontal inhomogeneities in vapour and temperature distributions. One can readily see from Extended Data Fig. 3a that the 3D model always predicts lower temperatures than the 1D one. As a result, runaway greenhouse occurs at much higher insolation.

The explanation for this fact can be found in Extended Data Figs 3 and 4. Indeed, as observed on the Earth, subtropical regions of the troposphere are unsaturated[17,18]. As a result, these regions can emit more thermal flux than the asymptotic limiting flux (Extended Data Fig. 4b). At a given mean surface temperature, the global thermal flux can thus be larger than in the fully saturated 1D case, as can be seen in Extended Data Fig. 3b. To retrieve comparable results with the 1D model, we have to decrease the relative humidity in the radiative transfer to 0.6 for present-day Earth and ~0.45 near the runaway greenhouse limit. As a result, the fact that subtropics both are unsaturated and seem to get dryer under an increased insolation strongly stabilizes the climate. Thus, as on the Earth today, subtropics will continue to play the part of radiative fins[18], deferring catastrophic consequences of a runaway greenhouse further in the future.

In the context of the runaway greenhouse, the effect of this lack of saturation has been recognized in ref. 19, where the authors performed a highly idealized numerical experiment. They found that their 3D results could be mimicked in 1D by forcing a relative humidity of 0.6, or a little less, throughout the atmosphere. However, because of their use of a cloud-free, grey radiative transfer and of a very crude description of the water cycle, they were unable to make a quantitative assessment of the runaway greenhouse insolation limit for a more realistic cloudy, non-grey atmosphere. Indeed, this limit is directly determined by the grey opacity used, which is a free parameter. In terms of relative humidity, however, these authors find values and trends that are roughly similar to ours. Considering the very different set-up involved (no ground thermal inertia, no seasonal or diurnal variations, etc.), this suggests that, at least when looking at rough mean values, the mechanisms controlling the evolution of the relative humidity should be controlled by relatively simple processes[17]. On the contrary, even if their very different temperature profiles, due to the grey approximation (especially their warm stratospheres), should not affect the runaway greenhouse threshold, they certainly prevent any robust conclusion considering water escape.

Finally, another result of our simulations is to confirm that both cloud- and ice-albedo feedbacks are destabilizing in the runaway greenhouse context. Indeed, because we keep the surface albedo fixed to a higher value than on the Earth today to mimic the present effect of both ice and clouds, this set of simulations can be seen as a case where clouds and ice are present but have no feedback. In this case, as visible in Extended Data Fig. 3a, runaway occurs at a flux greater than ~400 W m^{-2}, which is much higher than the ~375 W m^{-2} found when the cloud feedback is accounted for.

Stratospheric temperatures in non-grey atmospheres. One might be surprised by the fact that the stratospheric temperature found in our baseline model (Fig. 3) can be much colder than the skin temperature, $T_{skin} = T_{eq}/2^{1/4}$, where $T_{eq} \equiv [(1-A)F_\star/\sigma]^{1/4}$ is the equilibrium temperature, A is the bond albedo, $F_\star$ is the mean insolation and σ is the Stefan–Boltzmann constant.

The reason for the existence of a skin temperature in grey atmospheres is that there is, by construction, no radiative window by which the lower atmosphere and surface can cool to space without interacting with the upper atmosphere. The radiative equilibrium thus implies that the upward and downward emission from the optically thin upper atmosphere must both be equal to half the absorption of upward infrared flux, explaining the usual $2^{-1/4}$ factor.

As extensively discussed in ref. 14, in reality the radiation illuminating the upper atmosphere is depleted in the portion of the spectrum that is efficiently absorbed by the gas in the troposphere. The stratosphere, which, by definition, can efficiently absorb the upwelling infrared radiation only in this part of the spectrum, is thus poorly heated from below. However, it is still able to radiate efficiently, and is thus forced to cool to maintain radiative equilibrium balance. This does not threaten the global radiative balance of the whole atmosphere because even if the upwelling flux is small in the opaque regions of the troposphere, the surface and lower troposphere can cool through the transparent radiative windows.

A first quantitative, analytical estimate of the magnitude of this effect can be done using an idealized 1-band gas, that is, a gas absorbing only in one narrow wavelength region. As described in ref. 14, this simple model already shows that the ratio T_{skin}/T_{eq} can be lower than inferred in the grey case. A much more comprehensive quantification of this phenomenon using an idealized (in the sense that the line shape can be chosen arbitrarily) semi-analytical non-grey radiative model has been provided in ref. 21. The main conclusions of that study was that in a non-grey atmosphere, the temperature increases with increasing mean opacity below a certain height and decreases with increasing mean opacity above that height. It also found that there is no lower limit to the temperature at the top of the atmosphere: it can approach zero arbitrarily closely as the width of the lines is decreased.

Although the aforementioned studies demonstrate that there is no theoretical paradox in having (arbitrarily) cold stratospheres, we now turn to the validation of our more realistic radiative transfer model in the case of our ozone-free, Earth-like planet. Recently, several different climate models (mainly addressing early Earth climate), have computed temperature profiles for an ozone-free atmosphere under present insolation. Among these, ref. 44 finds a minimum stratospheric temperature of 140–145 K, and ref. 45 finds it to be around 150 K. In a more idealized, 1D set-up, the authors of ref. 22 have published consistently computed 1D temperature profiles for N_2–CO_2–H_2O atmospheres and they also find stratospheric temperatures of around 140–150 K. Considering the fact that, within the uncertainties, our estimation for the ozone-free stratospheric temperature (~140 K) agrees well with these numerous published results, which use different numerical models, we are confident that our non-grey radiative transfer model is suitable for the present application.

30. Mellor, G. L. & Yamada, T. Development of a turbulence closure model for geophysical fluid problems. *Rev. Geophys. Space Phys.* **20,** 851–875 (1982).
31. Rothman, L. S. *et al.* The HITRAN 2008 molecular spectroscopic database. *J. Quant. Spectrosc. Radiat. Transf.* **110,** 533–572 (2009).
32. Clough, S., Kneizys, F. & Davies, R. Line shape and the water vapor continuum. *Atmos. Res.* **23,** 229–241 (1989).
33. Borysow, A. & Frommhold, L. Collision-induced rototranslational absorption spectra of N_2-N_2 pairs for temperatures from 50 to 300 K. *Astrophys. J.* **311,** 1043–1057 (1986).
34. Richard, C. *et al.* New section of the HITRAN database: collision-induced absorption (CIA). *J. Quant. Spectrosc. Radiat. Transf.* **113,** 1276–1285 (2011).
35. Toon, O. B., McKay, C. P., Ackerman, T. P. & Santhanam, K. Rapid calculation of radiative heating rates and photodissociation rates in inhomogeneous multiple scattering atmospheres. *J. Geophys. Res.* **94,** 16287–16301 (1989).
36. Hansen, J. E. & Travis, L. D. Light scattering in planetary atmospheres. *Space Sci. Rev.* **16,** 527–610 (1974).
37. Bucholtz, A. Rayleigh-scattering calculations for the terrestrial atmosphere. *Appl. Opt.* **34,** 2765–2773 (1995).
38. Le Treut, H. & Li, Z.-X. Sensitivity of an atmospheric general circulation model to prescribed SST changes: feedback effects associated with the simulation of cloud optical properties. *Clim. Dyn.* **5,** 175–187 (1991).
39. Manabe, S. & Wetherald, R. T. Thermal equilibrium of the atmosphere with a given distribution of relative humidity. *J. Atmos. Sci.* **24,** 241–259 (1967).
40. Frierson, D. M. W. The dynamics of idealized convection schemes and their effect on the zonally averaged tropical circulation. *J. Atmos. Sci.* **64,** 1959–1976 (2007).
41. Boucher, O., Le Treut, H. & Baker, M. B. Precipitation and radiation modeling in a general circulation model: Introduction of cloud microphysical processes. *J. Geophys. Res.* **100,** 16395–16414 (1995).
42. Forget, F., Hourdin, F. & Talagrand, O. CO_2 snowfall on Mars: simulation with a general circulation model. *Icarus* **131,** 302–316 (1998).
43. Van Leer, B. Towards the ultimate conservative difference scheme: IV. A new approach to numerical convection. *J. Comput. Phys.* **23,** 276–299 (1977).
44. Le Hir, G., Teitler, Y., Fluteau, F., Donnadieu, Y. & Philippot, P. The faint young Sun problem revisited with a 3-D climate-carbon model - Part 1. *Clim. Past Discuss.* **9,** 1509–1534 (2013).
45. Wolf, E. & Toon, O. B. Hospitable Archean climates in a general circulation model. *Astrobiology* **13,** 656–673 (2013).

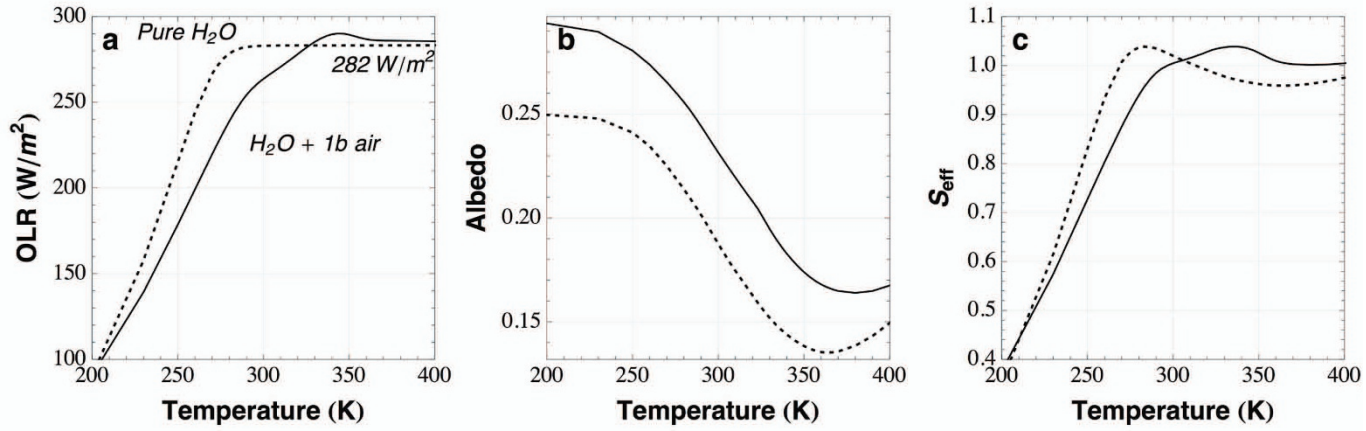

Extended Data Figure 1 | Validation of the radiative transfer model at high temperature. Dependence of outgoing thermal radiation (**a**), Bond albedo (**b**) and effective solar constant (with respect to the current solar constant; **c**) on surface temperature with a 1D version of our GCM in the 'reverse climate modelling' mode[4,6]. The dashed curve is the pure-water case, and the solid curve is the case with a 1 bar N_2 background atmosphere including 376 p.p.m.v. of CO_2. The surface albedo is 0.25.

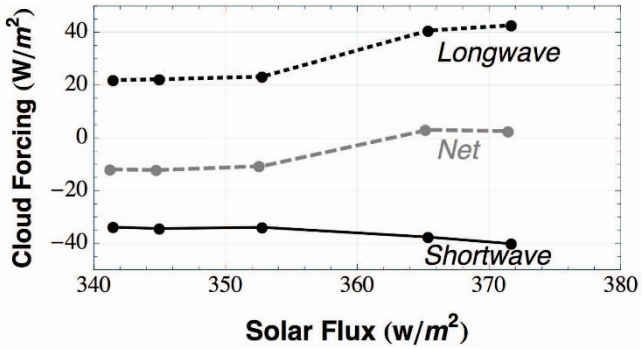

Extended Data Figure 2 | Evolution of the cloud radiative forcing with mean solar incoming flux for the scenario with fixed cloud particle radii. Solid, dotted and dashed curves are respectively the short-wave, long-wave and net radiative cloud forcing. Although fewer simulations have been run, the changes in the value of the slopes around 353 and 365 W m^{-2} seem to have the same origin as the behaviour change seen in Fig. 2c (although they occur at different fluxes). These changes in cloud behaviour might be due to the disappearance of both permanent ice caps (at lower fluxes) and seasonal snow cover (at higher fluxes).

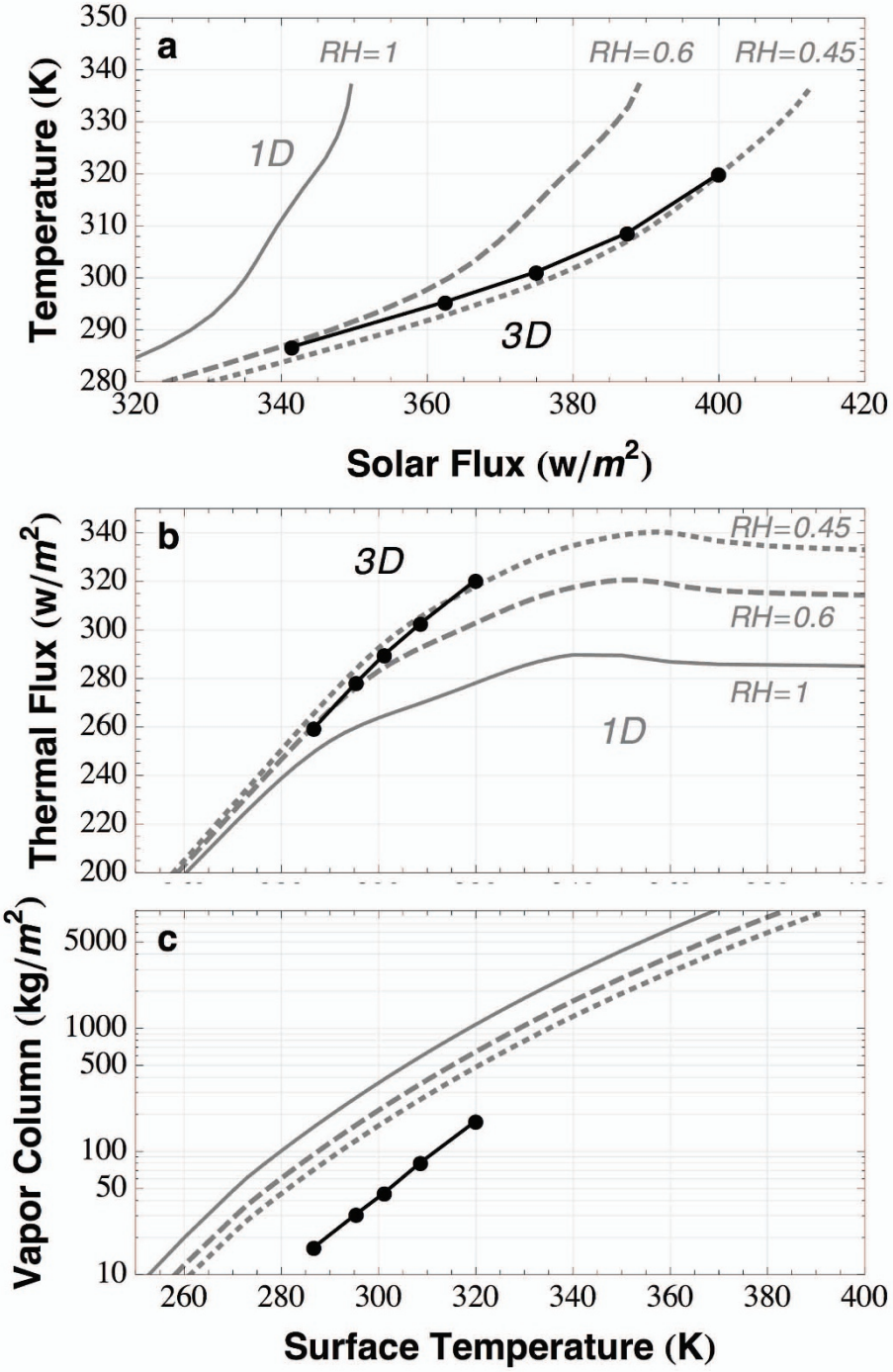

Extended Data Figure 3 | Comparison between 1D and 3D cloud-free aquaplanet simulations. **a**, Mean surface temperature as a function of incoming stellar flux. **b**, Emitted thermal flux dependence on surface temperature. **c**, Water-vapour column as a function of surface temperature. In all panels, filled dots stand for the idealized 3D set of aquaplanet simulations, and grey curves stand for the 1D model. In both cases, a uniform surface albedo of 0.22 is used. In the 1D case, three values of relative humidity in the radiative transfer are used: 1 (solid), 0.6 (dashed) and 0.45 (dotted).

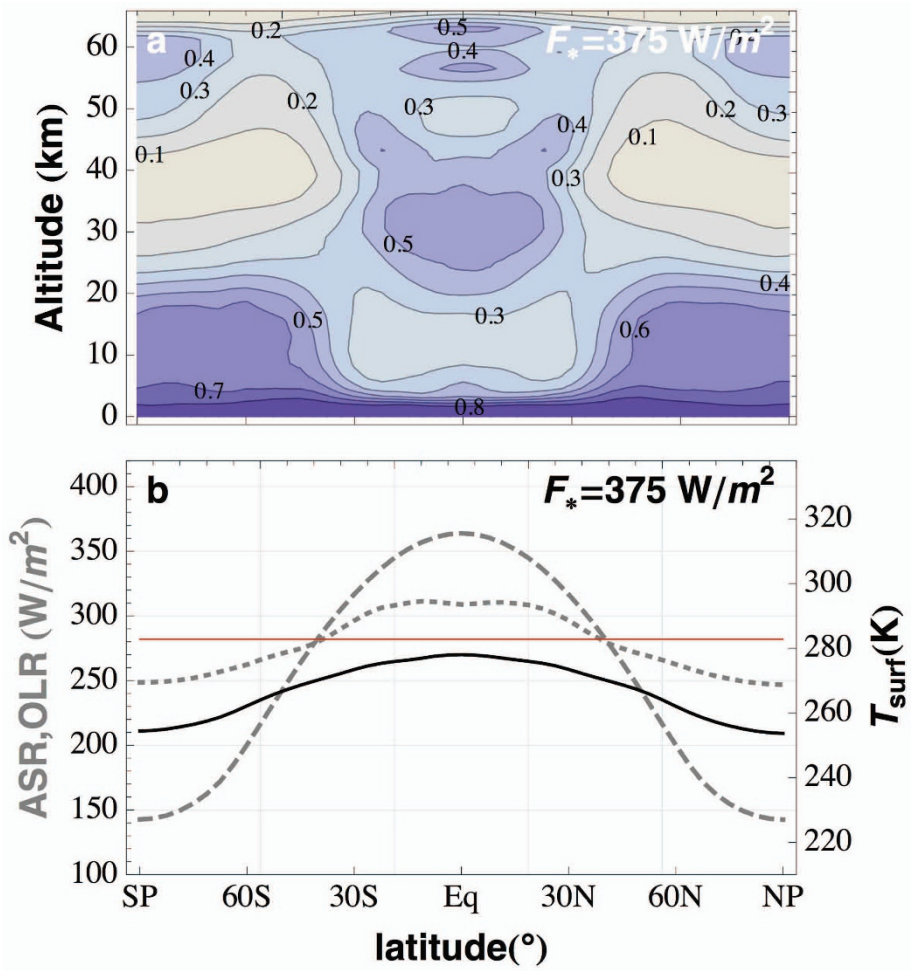

Extended Data Figure 4 | Relative humidity and radiative budget for an idealized, cloud-free aquaplanet. **a**, Annually and zonally averaged relative humidity in a latitude–altitude plane. **b**, Distributions of absorbed (grey dashed) and emitted (grey dotted) flux and surface temperature (solid black) with latitude (annually and zonally averaged). The red line is the asymptotic-limit infrared flux for a saturated atmosphere. Results are shown for the case with insolation 375 W m^{-2}.

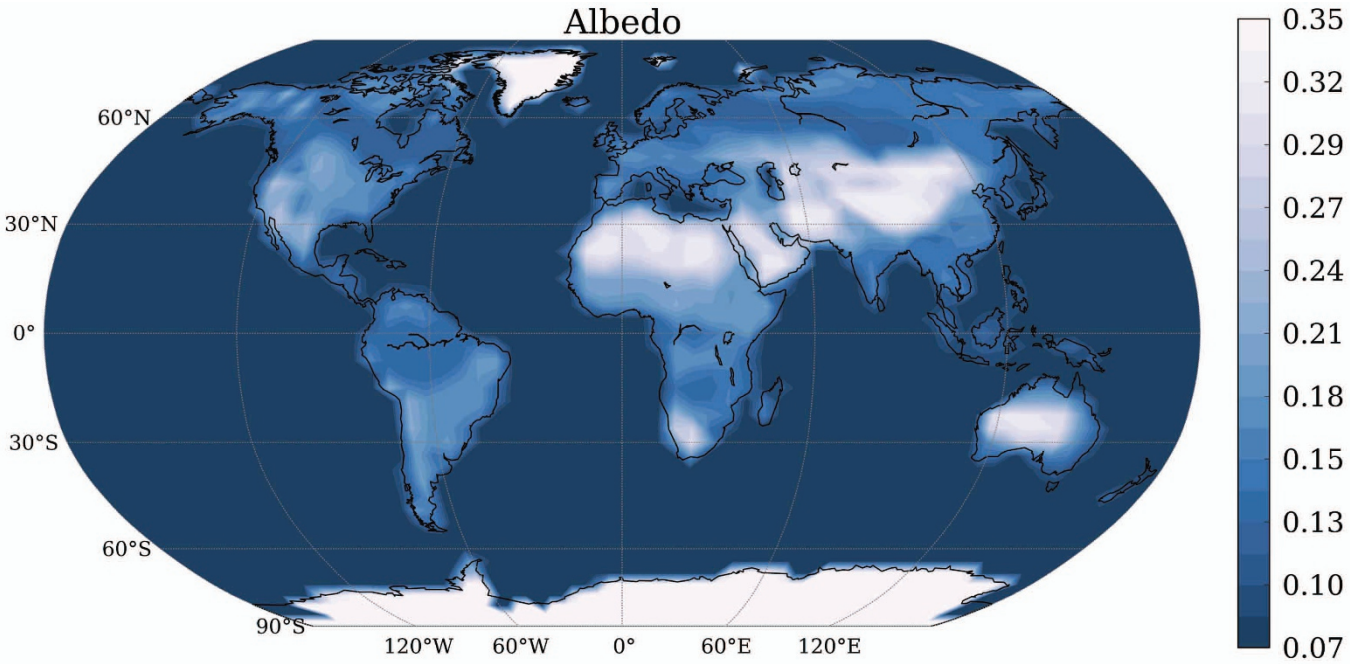

Extended Data Figure 5 | Surface albedo map used for the Earth baseline case. This map does not include the effect of the ice albedo, which is computed directly by the GCM. The albedo of Greenland and Antarctica, in particular, was set to 0.35. The altitude of these regions was, however, left unchanged, explaining in part the temperature contrasts around these areas in Fig. 1.